

Noname manuscript No.
(will be inserted by the editor)

**1 Significant wind disturbances induced by giant
2 dunes.**

**3 Cyril Gadal · Pauline Delorme ·
4 Clément Narteau · Giles Wiggs ·
5 Matthew Baddock · Joanna M. Nield ·
6 Philippe Claudin**

7
8 Received: DD Month YEAR / Accepted: DD Month YEAR

9 Abstract

10 abstract

11 Keywords Boundary layer · Turbulent flow · Sand dunes · Fluide-structures
12 interactions

C. Gadal

Institut de Mécanique des Fluides de Toulouse (IMFT), Université de Toulouse, CNRS,
INPT, UPS, Toulouse, France
E-mail: cyril.gadal@imft.fr

S. Author
second address

T. Author
third address

13 1 Introduction

14 Whenever a flow encounters an obstacle, various types of interactions can arise
15 depending on the different time and length scales involved. In the case of atmo-
16 spheric flows, this depends mainly on the part of the vertical structure of the
17 atmosphere, schematically composed of a turbulent boundary layer topped by
18 a turbulence-free part, with which the obstacle interacts (Stull 1988). At the
19 largest scale, the feedback of mountains on the stratified flow of the free at-
20 mosphere results in wave generation as well as significant wind disturbances,
21 such as foehn winds in the lee side (?). Inside the boundary layer, the inter-
22 action between a turbulent flow and hilly surfaces is for example key to the
23 understanding ocean surface wind-driven waves, or eolian bedforms in desert
24 (Belcher and Hunt 1998; Sullivan and McWilliams 2010; Courrech du Pont
25 2015).

26 Indeed, eolian sand dunes typically emerge from the interaction by the
27 turbulent flow and the topography (Charru et al. 2013). Later on, when the
28 dune reaches an intermediate size, it may induce large deflections that can
29 significantly impact sediment pathways of coastal systems (Hesp et al. 2015).
30 Likewise, the collective behavior of dune populations may also be affected by
31 long-range interactions due to flow disturbances induced by each individual
32 (Smith et al. 2017; Bacik et al. 2020). As the dunes increase in size by collisions
33 and coarsening, they sometimes reach a giant size, comparable to the boundary
34 layer depth, thus inducing interactions not only with the turbulent flow of the
35 ABL, but also with the free atmosphere (Andreotti et al. 2009). However, the
36 wind disturbances induced by these giant dunes have never been quantified.

37 The study of the impact of obstacles on the atmospheric flows allows its
38 incorporation within meteorological numerical model. Therefore, they mainly
39 become limited by the precision of the included topographical data, as well
40 as the spatial grid of the model. For example, the latest climate reanalysis,
41 ERA5-Land, is limited by its 9 km spatial resolution, while including the
42 data 30-m Digital Elevation Models (DEMs) of the shuttle radar topography
43 mission (Farr et al. 2007; Muñoz-Sabater et al. 2021). As such, it can not
44 reproduce the flow disturbances induced by giant dunes, which have a typical
45 length scale ~ 1 km.

46 Here, we compare the wind predictions from the ERA5-Land dataset to
47 local measurements in four different places across the Namib desert. In places
48 with no significant topographies smaller than the model grid, we show that
49 both wind datasets agree with each other. On the contrary, in places with
50 giant dunes, we show that they may differ for some specific meteorological
51 conditions, that we link to the circadian cycle of the ABL. We thus highlight
52 the importance of the mid-scale topographies for local wind regimes, and its
53 implications in the case of sand seas for smaller-scale eolian bedforms.

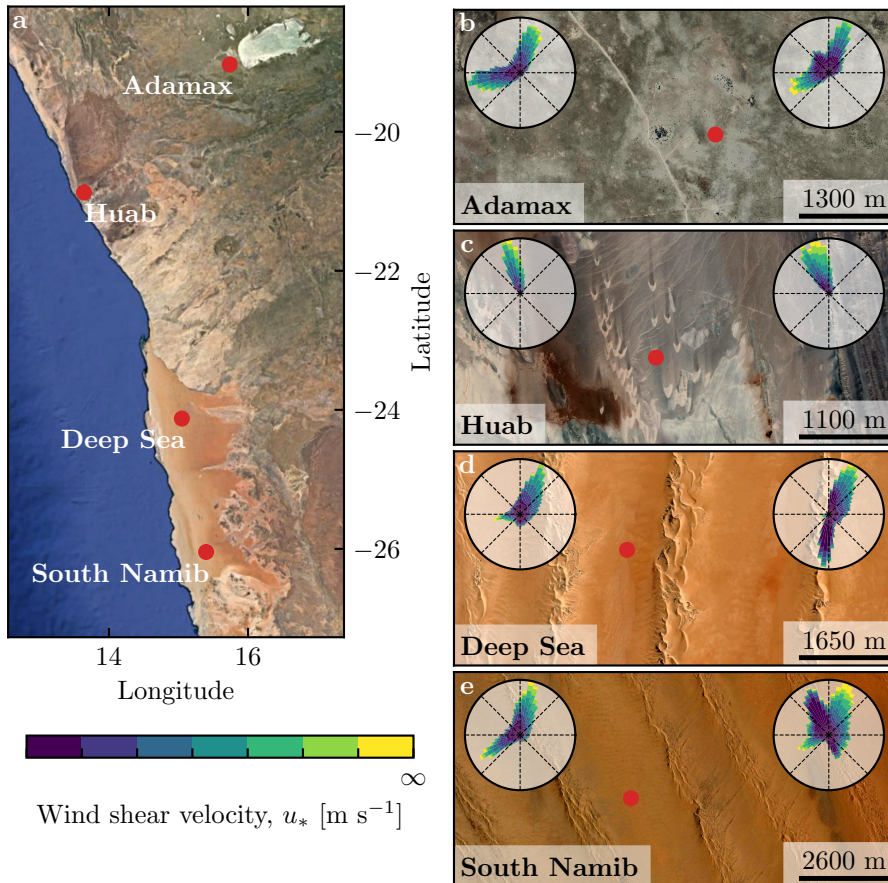


Fig. 1 Wind data used in this study **a**: Location of the studied sites. **b–e**: Satellite images of the studied sites (Google-Earth, Maxar Technologies, CNES/Airbus). In each subplot, the left and right wind roses represent the data from the ERA5Land climate reanalysis and the in situ stations, respectively. Note that the bars show the direction towards which the wind blows. The red dots show the location of the in situ stations.

54 2 Wind regimes across the Namib Sand Sea

55 2.1 Datasets

56 Two wind datasets are used in this study. First, local winds are provided by
 57 stations situated in different environments (see Fig. 1). The wind strength and
 58 direction are measured every 10 minutes by cup anemometers and wind vanes,
 59 at heights between n and n meters depending on the station. The available
 60 period of measurements ranges from 1 to 5 discontinuous years distributed
 61 between 2012 and 2020 (see Fig. S1). We checked that at least one complete
 62 seasonal cycle is available at each station. Then, regional winds are extracted
 63 at the same locations and periods from the ERA5-Land dataset, which is a

replay at a smaller spatial resolution of ERA5, the latest climate reanalysis from the ECMWF (Hersbach et al. 2020; Muñoz-Sabater et al. 2021). It provides hourly estimates of the 10-m wind velocity and direction at a spatial resolution of ~ 9 km ($0.1^\circ \times 0.1^\circ$).

For comparison, the local measurements are averaged into 1-hr bins centered on the temporal scale of the ERA5-Land estimates (see Fig. S2). As the wind velocities of both datasets are provided at different heights, we convert them into shear velocities (see SI section ??), characteristic of the whole turbulent wind profile within the atmospheric boundary layer, which are then used together with the wind direction for further analysis. The resulting wind data are shown on the wind roses of Fig. 1(b–e).

Finally, the dune properties are computed using an autocorrelation method from the 30-m Digital Elevation Models (DEMs) of the shuttle radar topography mission (Farr et al. 2007). For the South Namib and Deep Sea stations, we obtain respectively orientations of 85° and 125° , wavelengths of 2.6 km and 2.3 km and amplitudes of 45 m and 20 m (see SI for additional details).

2.2 Agreement between local and regional winds

The regional wind patterns in the Namib are strongly controlled by the sea breeze, resulting in strong northward components present in all regional wind roses of figure 1, also deviated by the large scale topography (Lancaster 1985). These daily winds are the strongest during the second-half of the year (September–January). In winter, an additional easterly component can be recorded during the night, induced by the combination of katabatic winds forming on the mountains, and infrequent ‘berg’ winds, which are responsible of the high wind velocities observed (Lancaster 1984). The frequency of these easterly components decreases from the inland to the coast, resulting in three bidirectional wind regimes within the Namib Sand Sea and at the Adamax salt pan (Fig. 1(c, d, e)) and one unidirectional wind regime on the coast at the outlet of the Huab River.

In the case of the Adamax and Huab stations, these regional wind roses qualitatively matches their respective in situ local measurements. However, for the Deep Sea and South Namib stations, the local wind roses exhibit additional components aligned with the giant dune orientation visible on the satellite images.

Indeed, the analysis of the wind speed and direction time series shows that the matching between the local and regional winds is verified for the stations with flat environment at all times (Fig. 2(a–b)), as well as for the stations within the giant dune field, but only during September–January (Fig. 2(c–d)). This agreement is statistically verified, as shown by the Fig. S5.

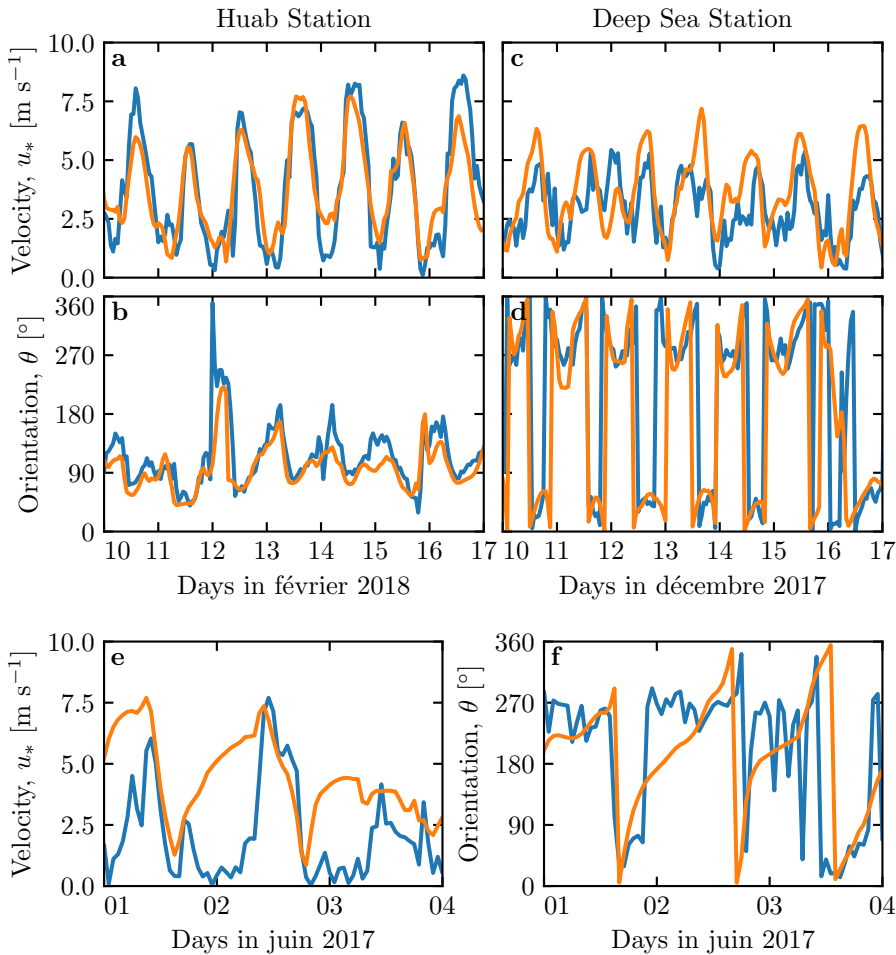


Fig. 2 Temporal comparison between the wind data coming from the Era5Land climate reanalysis (orange lines) and from the in situ measurements (blue lines). **a–b:** Huab station. **c–d:** Deep Sea station in winter. **e–f:** Deep Sea station in summer.

103 2.3 Influence of the giant dunes on local wind regimes

104 In winter, the local and regional winds match only during the morning for
 105 the stations within the giant dune field, when the southerly/southwesterly
 106 sea breeze dominates (see Fig. 2(e–f), Fig. 3 and Fig. S6). In the late after-
 107 noon and during the night, when the northwesterly ‘berg’ and katabatic winds
 108 blow, the two datasets differ. More specifically, this mismatch mainly occurs
 109 during at low wind velocities. In this case, the angular wind distribution of
 110 the local measurements exhibits two additional modes separated of $\simeq 180^\circ$,
 111 each corresponding to the giant dune alignment (purple frame in Fig. 3 and
 112 Fig. S6). This deviation at low wind velocities is statistically verified, and is

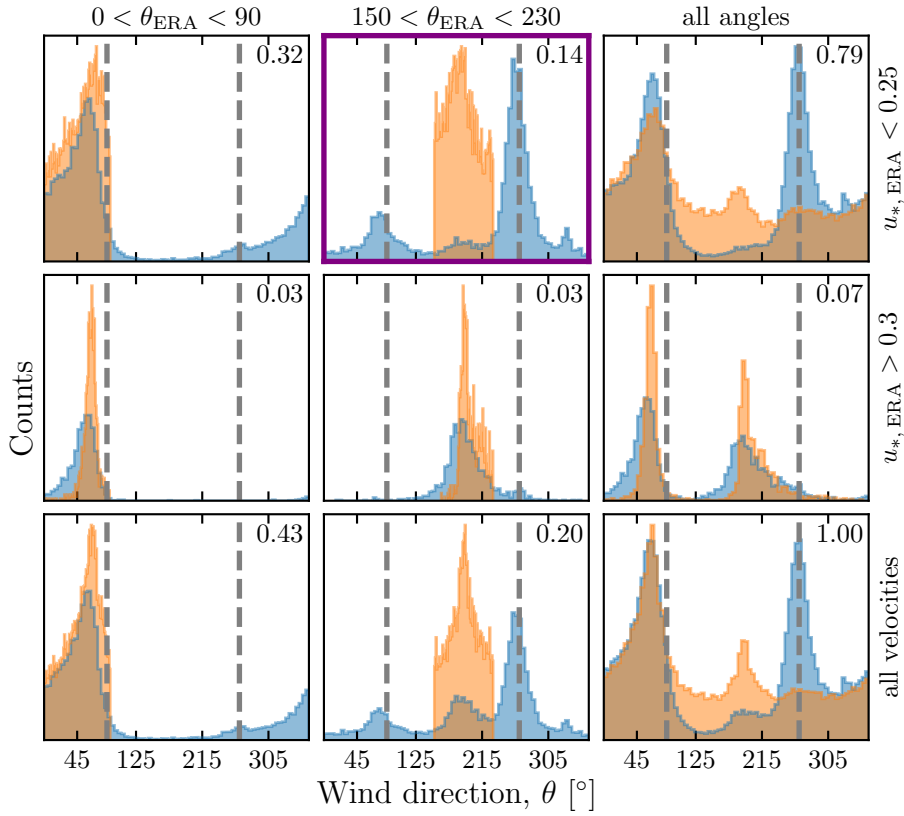


Fig. 3 Distributions of wind direction at the Deep Sea Station for the Era5Land climate reanalysis (orange) and the in situ measurements (blue). In each subplot, both distributions are plotted from the same time steps, selected with constraints on the wind direction (columns) and/or wind velocity (rows) in the Era5Land dataset. The vertical gray dashed lines indicate the dune orientation, and the top right numbers the percentage of the total number of time steps selected in each subplot. The purple frame highlights the regime (small wind velocities, nocturnal summer wind) during which the wind data from both datasets differs. A similar figure can be obtained for the Deep Sea station (see Fig. S6).

¹¹³ also associated with a global attenuation of the wind strength (Fig. S6 and
¹¹⁴ Fig. S7).

¹¹⁵ **3 Influence of the circadian cycle of the atmospheric boundary ¹¹⁶ layer**

¹¹⁷ Previous studies have linked meteorological flow around and over obstacles
¹¹⁸ to the vertical structure of the atmosphere (Stull 1988). At the dune scale,
¹¹⁹ its lower part, the turbulent atmospheric boundary layer (ABL), is directly
¹²⁰ influenced by the planetary surface (Stull 1988). When the latter is warmer
¹²¹ than the ambient air (typically during the day), a strong convection takes

place, resulting in a logarithmic wind profile and a vertically constant potential temperature θ (which corresponds to the air density corrected from the vertical pressure variation). During the night, the surface cools faster than the ambient air, which can result in a stable layer close to the surface (typically the first 200 meters). Above, the free atmosphere (FA) is a stably stratified zone in which turbulence is negligible, and where the flow is usually considered as incompressible and inviscid. In the middle, a transitional layer, also known as entrainment zone, is characterized by a sharp increase of the potential temperature, which traps turbulence resulting from the surface friction below it. As it is much shallower than the other two layers, we consider it as capping singularity inducing a discontinuity in the potential temperature profile.

3.1 Relevant non-dimensional parameters and physical modeling

As a result, the giant dunes evolve in a turbulent flow capped by a stratified atmosphere, with a transitional layer acting as a free surface in between. When the dune are small enough, typically in the case of dune emergence or early coarsening (Fig. 4b), they do no interact with the top of the ABL (Fourriere et al. 2010). However, the giant dunes present in the Deep Sea and South Namib stations have wavelengths comparable or larger than typical ABL depths, inducing their interaction with the capping layer and the free atmosphere above (Andreotti et al. 2009). However, as sketched in Fig. 4c–d, the nature of this interaction depends on two non-dimensional number, both called Froude numbers in the literature (Vosper 2004; Sheridan and Vosper 2006; Hunt et al. 2006; Jiang 2014).

The ability of the capping layer to deform under the presence of an underlying topography is controlled by the *surface Froude number*, typically used in the context of bedforms in rivers (Fourriere et al. 2010; Andreotti et al. 2012):

$$\mathcal{F}r_S = \frac{U}{\sqrt{\frac{\Delta\rho}{\rho} g H}}, \quad (1)$$

where U is the wind velocity at the top of the ABL, H its depth, ρ its average density and $\Delta\rho$ the density jump between the ABL and the FA. Likewise, the FA stratification ability to deform is controlled by the *internal Froude number*, typically used in the context of flow disturbances induced by mountains (Stull 1988):

$$\mathcal{F}r_I = \frac{U}{HN}, \quad (2)$$

where N is the Brunt-Väisälä frequency, characteristic of a stratified fluid. When the flow inertia dominates over its weight ($\mathcal{F}r_S \gg 1$) and the weight of the stratification ($\mathcal{F}r_I \gg 1$), both the capping layer and the stratification deform and adapt to the underlying topography (Fig. 4d), resulting in an unconfined flow (?). However, an opposite force balance induces a rigid capping layer and/or stratification (Fig. 4c), resulting in confined flows. In this case,

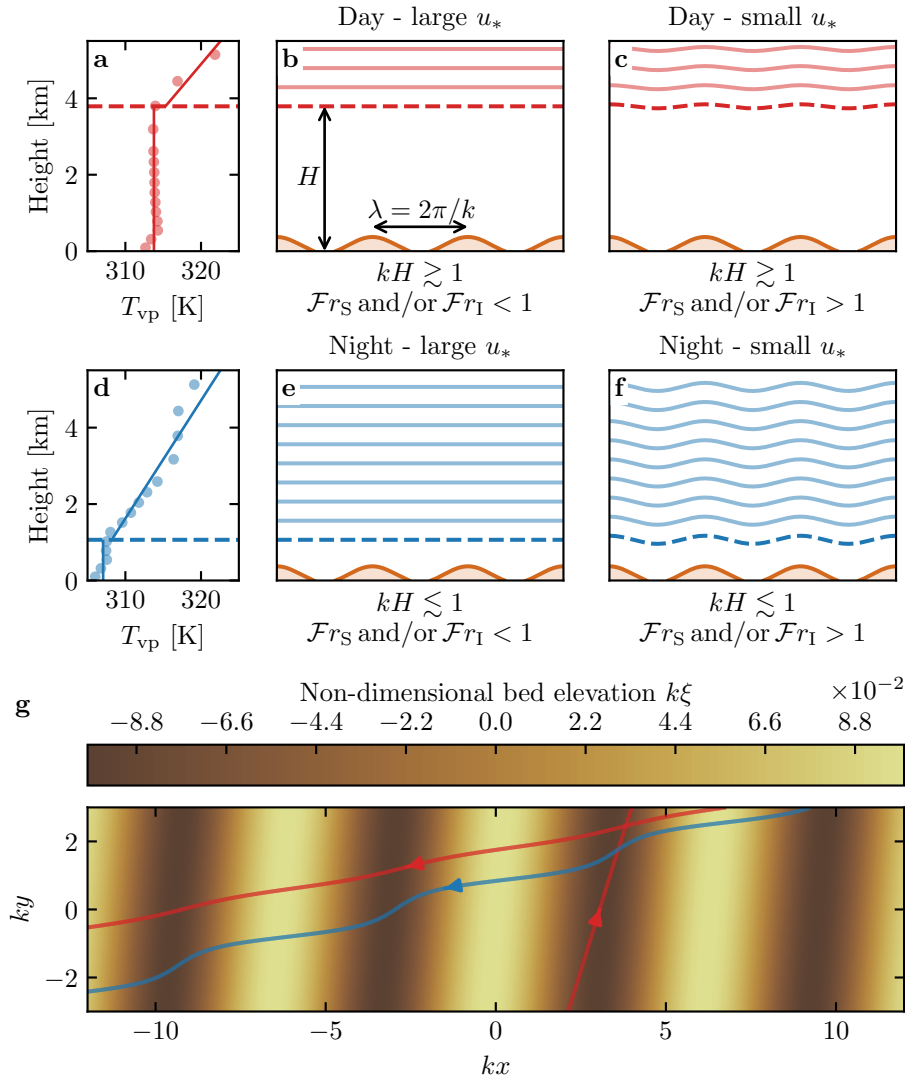


Fig. 4 **a:** Vertical profiles of the virtual potential temperature at 2 different time steps (blue - 29/11/2012 - 1100 UTC, red - 21/03/2017 - 1200 UTC) at the Deep Sea station. Dots: data from the ERA5 reanalysis. Transparent dashed lines: boundary layer height given by the ERA5 reanalysis, calculated from the bulk Richardson number (Seidel et al. 2012). Plain lines: vertical (boundary layer) and linear (free atmosphere) fits to estimate the stratification properties. **b-d:** Sketches representing the interaction between the giant dunes and the atmospheric flow for different meteorological conditions. **e:** Streamlines qualitatively representing the effect of flow confinement, in the case of the Deep Sea station. The red and straight blue lines are calculated from the unconfined case, representing the situations **b-c**. The sinuous blue line represents the confined case of **d**. For details on their derivation, see Appendix.

159 the confined flow has trouble going smoothly over the obstacle, and are then
 160 typically associated with large deviations and modulation of the wind velocity,
 161 as qualitatively illustrated in the case of the Deep Sea station by Fig. 4e (?).

162 **3.2 Flow regime diagrams**

163 In the spirit of Sheridan and Vosper (2006), we aim to compute flow regime
 164 diagrams in the space defined by the three relevant non-dimensional numbers
 165 presented above, (kH , \mathcal{Fr}_S , \mathcal{Fr}_I). They are calculated from the time series of
 166 the geopotential, temperature and specific humidity vertical profiles available
 167 in the ERA5 climate reanalysis (see SI ??). The relative velocity modulation
 168 is computed as

$$\delta_u = \frac{u_*^{\text{ERA}} - u_*^{\text{station}}}{u_*^{\text{ERA}}}, \quad (3)$$

169 and the flow deviation as the minimal angle between the wind orientation in
 170 the two datasets:

$$\delta_\theta = |\min([\theta_{\text{ERA}} - \theta_{\text{station}}] \bmod 360, [\theta_{\text{station}} - \theta_{\text{ERA}}] \bmod 360)|, \quad (4)$$

171 When these two variables are represented in the marginal spaces (kH , \mathcal{Fr}_S)
 172 and (kH , \mathcal{Fr}_I), different regime emerges (Fig. 5). The small wind disturbances
 173 ($\delta_\theta \rightarrow 0$, $\delta_u \rightarrow 0$) are located in the top-right part of the diagrams, corre-
 174 sponding to a regime mixing low-interactions (kH large enough, Fig. 4b) and
 175 low-confinement (\mathcal{Fr}_S , \mathcal{Fr}_I large enough, Fig. 4c).

176 Lower values of kH (stronger interaction) or Froude numbers (stronger
 177 confinement) then both leads to an increase in wind disturbances, both in
 178 terms of orientation and velocity. Interestingly, the limit of no-interactions be-
 179 tween the topography and the boundary layer structure ($kH \gg 1$), in which
 180 the properties of the capping layer and the stratification become irrelevant
 181 (Fig. 4b–4c), is never reached here, in the case of giant dunes. Below a thresh-
 182 old value of $kH \simeq 0.3$, wind disturbance occurs independently of the Froude
 183 numbers value. However, the latter seem to control a transition between from
 184 damped to amplified wind velocities within the interdune (Fig. 5c–5d), for
 185 which we do not have an explanation.

186 **4 Discussion**

187 The comparison of local and regional wind data gives a direct evidence of the
 188 giant dunes feedback on the flow. In flat areas, the matching between both
 189 datasets highlights the ability of the latest generation of climate reanalysis to
 190 predict the wind flow up to scales ~ 10 km, i.e the grid model. When smaller
 191 scale topographies are present (giant dunes in our case), locally measured wind
 192 regimes may significantly differ from the regional ones. Furthermore, we link
 193 these disturbances induced by the dunes to their interaction with the lower

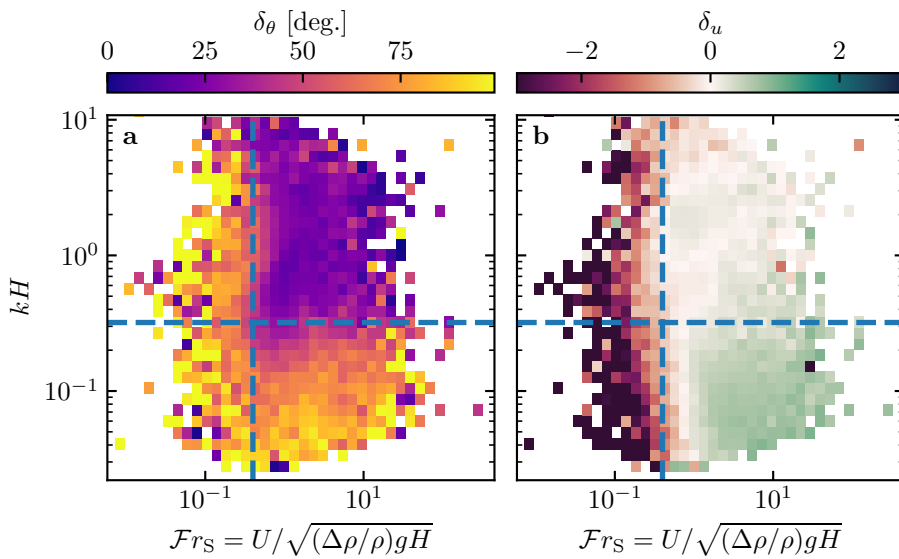


Fig. 5 Regime diagrams of the wind deviation δ_θ and relative attenuation/amplification δ_u in the space (\mathcal{Fr}_S, kH) , containing the data from both the Deep Sea and South Namib stations. Blue dashed lines empirically delimit the different regimes. The point density in each bin of the diagrams is shown in Fig. S11. The regime diagrams in the spaces (\mathcal{Fr}_I, kH) and $(\mathcal{Fr}_I, \mathcal{Fr}_S)$ are shown in Fig. S12.

part of the atmospheric vertical structure, and more specifically to its circadian variability. During the day, the top of the ABL is high enough to limit the interaction of the capping layer and the FA stratification with the giant dunes, resulting in a low flow confinement, and thus small wind disturbances. During the night, the small ABL height induces a stronger flow confinement, associated with large wind deviation and acceleration or deceleration. Interestingly, we also found that this effect could be counterbalanced by the presence of large wind velocities, capable of deforming the capping layer and/or the FA stratification and thus decreasing the confinement effect.

Simple linear model such as the one of Andreotti et al. (2009) also suggests that larger wind disturbances occur under strong flow confinement such as described above. However, they are unable to reproduce the magnitude of the observed deviations, probably due to the presence of hydrodynamical non-linear effects, negligible in low confinement situations, but not otherwise (see Fig. S12 and Appendix 1). Another limit in the comparison between theoretical predictions and measured is induced by the single-point measurements. To have reliable representations of the flow structures related to wind disturbances, additional measurements in different places on and near the same topographical obstacle are needed.

This study highlights the interaction between giant dunes and the atmospheric boundary layer, thus supporting for example the way the capping layer acts as a bounding surface limiting dune growth (Andreotti et al. 2009; Gunn

et al. 2021). This interaction also have implications at smaller scales, where bedforms then develop from the disturbed wind instead of the regional one. Differences between larger and smaller scale (thus older and more recent) dune patterns are observed ubiquitously, and have sometimes in the literature been attributed to climatic changes in wind regimes (?). Here, we suggest using this feedback mechanism that current winds can explain dune patterns at all scales, such as the linear dunes (~ 50 m -wide) elongating within the interdune between two giant linear dunes (~ 2 km -wide) in the Namib Sand Sea (see Fig. 6).

Acknowledgements These should follow the concluding section of the paper and precede the References and any appendices, if they are present. The acknowledgements section does not require a section number.

Appendix 1: ABL turbulent wind model

Following the work of Fourriere et al. (2010) and Andreotti et al. (2012), we briefly expose in this section the linear response of a turbulent flow to a small aspect ratio perturbation of the topography ξ . As this topography can be decomposed into several sinusoidal modes, we focus on the response to a sinusoidal topography as:

$$\xi = \xi_0 \cos [k (\cos(\alpha)x + \sin(\alpha)y)], \quad (5)$$

which is also a good approximation to the giant dunes observed in the Deep Sea and South Namib Station (see Fig 1 and Fig S4). Here, x and y are the streamwise and spanwise coordinates, $k = 2\pi/\lambda$ the wavenumber of the sinusoidal perturbation, and α its crest orientation, calculated with respect to the y -direction.

In terms of basal shear stress $\tau = \rho u_*^2$, the flow response can then generally be written in as:

$$\tau_x = \tau_0 \left(1 + k \xi_0 \sqrt{\mathcal{A}_x^2 + \mathcal{B}_x^2} \cos [k (\cos(\alpha)x + \sin(\alpha)y) + \phi_x] \right), \quad (6)$$

$$\tau_y = \tau_0 k \xi_0 \sqrt{\mathcal{A}_y^2 + \mathcal{B}_y^2} \cos [k (\cos(\alpha)x + \sin(\alpha)y) + \phi_y], \quad (7)$$

where τ_0 is the basal shear stress on a flat bed, and $\phi_{x,y} = \tan^{-1} (\mathcal{B}_{x,y}/\mathcal{A}_{x,y})$. The in-phase and in-quadrature hydrodynamical coefficients $\mathcal{A}_{x,y}$ and $\mathcal{B}_{x,y}$ are functions of the flow conditions, i.e the bottom roughness, the free surface or the incident flow direction (Fourriere et al. 2010; Andreotti et al. 2009, 2012; Charru et al. 2013).

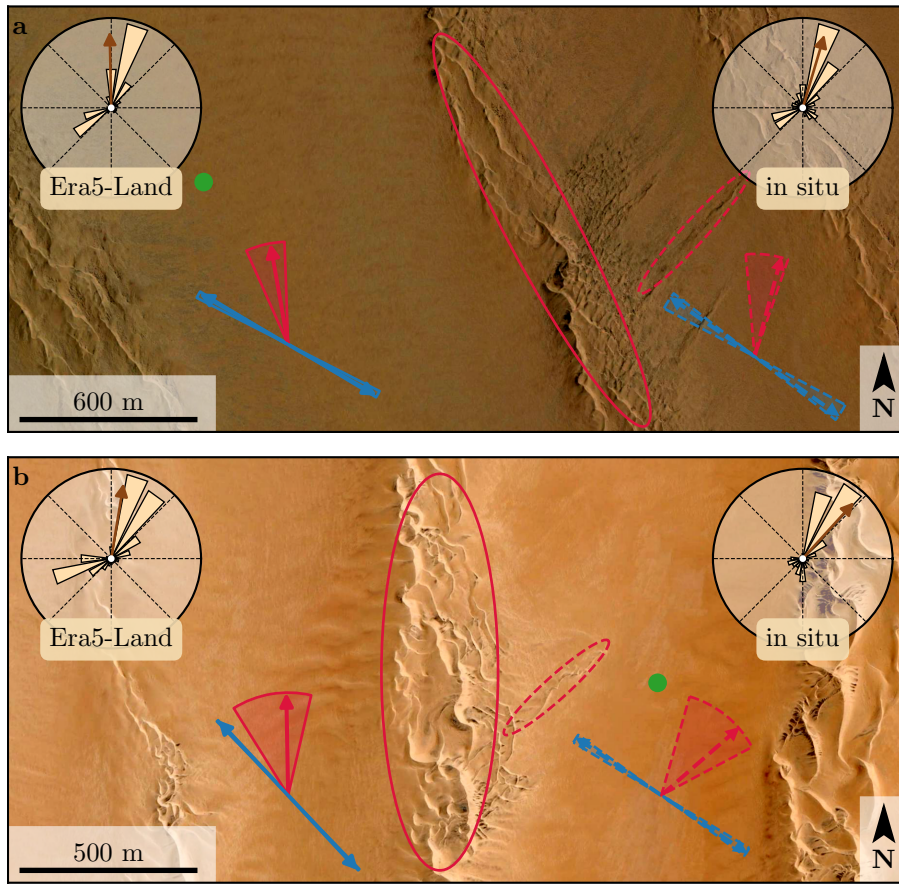


Fig. 6 Implications for smaller scale patterns in (a) the South Namib and (b) Deep Sea. The ellipses indicates the different types of elongating dunes, at large (plain) and small scale (dashed). The dune orientations are calculated using the model of ? from the sand flux angular distributions, shown here for typical sand quartz grains of 180 μm . The double blue and single red arrows correspond to the two possible dune growth mechanisms, bed instability and elongation, respectively. Likewise, plain arrows are calculated from the ERA5-Land datasets, and dashed arrows from the in situ measurements. Wedges show the uncertainty on the orientation calculation, and the arrows correspond to typical parameters found in the literature, i.e. a grain diameter of 180 μm and a flux-up ratio of 1.6. The green dots indicate the position of the measurement stations. See Appendix 2 for details.

Andreotti et al. (2012) have shown that the impact of the incident wind direction can be well approximated by the following expressions:

$$\mathcal{A}_x = \mathcal{A}_0 \cos^2 \alpha, \quad (8)$$

$$\mathcal{B}_x = \mathcal{B}_0 \cos^2 \alpha, \quad (9)$$

$$\mathcal{A}_y = \frac{1}{2} \mathcal{A}_0 \cos \alpha \sin \alpha, \quad (10)$$

$$\mathcal{B}_y = \frac{1}{2} \mathcal{B}_0 \cos \alpha \sin \alpha, \quad (11)$$

where \mathcal{A}_0 and \mathcal{B}_0 are now two coefficients independent of the dune orientation α . In the case of a fully turbulent boundary layer capped by a free atmosphere capping, they now only depend on kH , kz_0 , \mathcal{Fr}_I and \mathcal{Fr}_S , as detailed by Andreotti et al. (2009). More specifically, their variation in the marginal spaces (kH, \mathcal{Fr}_S) and (kH, \mathcal{Fr}_I) are shown in Fig. S12.

Typical values for the unconfined case are therefore $\mathcal{A}_0 = 3.4$ and $\mathcal{B}_0 = 1$. In our case of giant dunes with $k\xi_0 \sim 0.1$, significant wind disturbances are then expected when $\sqrt{\mathcal{A}_0^2 + \mathcal{B}_0^2} \sim 10$. However, this is also the limit of the linear regime where this theoretical model is applicable, as hydrodynamical non-linearities become significant when $k\xi_0\sqrt{\mathcal{A}_0^2 + \mathcal{B}_0^2} \sim 1$.

Appendix 2: Sediment transport and dune morphodynamics

Here, we briefly detail the sediment transport and dune morphodynamics theoretical framework leading to the prediction of sand fluxes and dune orientations from wind data.

The sediment fluxes can been directly linked to the wind basal shear stress at each time steps t from transport laws, whose exact forms depends on the sediment transport mechanisms taken into account. In this work, we following the recent work of Pähzt and Durán (2020), where the sediment flux q_{sat} on a flat bed made of loose sand can be expressed as:

$$\frac{q_{\text{sat},t}}{Q} = \frac{2\sqrt{\Theta_{\text{th}}}}{\kappa\mu} (\Theta_t - \Theta_{\text{th}}) \left(1 + \frac{C_M}{\mu} [\Theta_t - \Theta_{\text{th}}] \right), \quad (12)$$

where $\kappa = 0.4$ is the von Kármán constant, $C_M = 1.7$ a constant, $Q = d\sqrt{(\rho_s - \rho)gd/\rho}$ is a characteristic flux, with $\rho_s = 2.6 \text{ g cm}^{-3}$ and $d = 180 \mu\text{m}$ the grain density and diameter, and g the gravitational acceleration. The friction coefficient μ is taken to be the avalanche slope of the granular material, i.e. ~ 0.6 . Finally, the Shields number is defined as $\Theta = \rho u_{*,t}^2 / (\rho_s - \rho)gd$, and its threshold value for incipient sediment transport as been calibrated using laboratory experiments to $\Theta_{\text{th}} = 0.0035$.

The dune orientations are then predicted from the dimensional model of Courrech du Pont et al. (2014). The orientation α corresponding the bed instability is then the one that maximizes the following growth rate:

$$\sigma \propto \frac{1}{HW^T} \int_t q_{\text{crest},t} |\sin(\theta_t - \alpha)|, \quad (13)$$

where H and W are dimensional constants representing the dune height and width, respectively. The flux at the crest is expressed as:

$$q_{\text{crest},t} = q_{\text{sat},t} [1 + \gamma |\sin(\theta_t - \alpha)|], \quad (14)$$

where the flux-up ratio γ has been calibrated to 1.6 using field studies, underwater laboratory experiments and numerical simulations. Similarly, the dune

281 orientation corresponding to the elongation mechanism is the one that verifies:

$$\tan(\alpha) = \frac{\langle q_{\text{crest},t}(\alpha) \mathbf{e}_{\theta_t} \rangle \cdot \mathbf{e}_{WE}}{\langle q_{\text{crest},t}(\alpha) \mathbf{e}_{\theta_t} \rangle \cdot \mathbf{e}_{SN}}, \quad (15)$$

282 where $\langle \cdot \rangle$ denotes a vectorial time average. The unitary vectors \mathbf{e}_{WE} , \mathbf{e}_{SN} and
283 \mathbf{e}_{θ_t} are in the West–East, South–North and wind direction, respectively.

284 The computed dune orientations, blue and red arrows in figure 6, are how-
285 ever depending on a large number of parameters, for which we took typical
286 values for eolian desert on Earth. We therefore run a sensibility test by calculat-
287 ing the dune orientations for grain diameters ranging from $100 \mu\text{m}$ to $400 \mu\text{m}$
288 and the speed-up ratio from 0.1 to 10 (wedges on figure 6). We also checked
289 the sensibility the transport low by repeating the process with the quadratic
290 transport also used for comparison in Pähzt and Durán (2020), which led to
291 no more than $n\%$ of variation with respect to (12).

292 References

- 293 Andreotti B, Fourriere A, Ould-Kaddour F, Murray B, Claudin P (2009) Gi-
294 ant aeolian dune size determined by the average depth of the atmospheric
295 boundary layer. *Nature* 457(7233):1120–1123
- 296 Andreotti B, Claudin P, Devauchelle O, Durán O, Fourrière A (2012) Bedforms
297 in a turbulent stream: ripples, chevrons and antidunes. *Journal of Fluid
298 Mechanics* 690:94–128
- 299 Bacik KA, Lovett S, Colm-cille PC, Vriend NM (2020) Wake induced long
300 range repulsion of aqueous dunes. *Physical review letters* 124(5):054,501
- 301 Belcher SE, Hunt JCR (1998) Turbulent flow over hills and waves. *Annual
302 Review of Fluid Mechanics* 30(1):507–538
- 303 Charru F, Andreotti B, Claudin P (2013) Sand ripples and dunes. *Annual
304 Review of Fluid Mechanics* 45:469–493
- 305 Courrech du Pont S (2015) Dune morphodynamics. *Comptes Rendus Physique*
306 16(1):118–138
- 307 Courrech du Pont S, Narteau C, Gao X (2014) Two modes for dune orientation.
308 *Geology* 42(9):743–746
- 309 Farr TG, Rosen PA, Caro E, Crippen R, Duren R, Hensley S, Kobrick M,
310 Paller M, Rodriguez E, Roth L, et al. (2007) The shuttle radar topography
311 mission. *Reviews of geophysics* 45(2)
- 312 Fourriere A, Claudin P, Andreotti B (2010) Bedforms in a turbulent stream:
313 formation of ripples by primary linear instability and of dunes by nonlinear
314 pattern coarsening. *Journal of Fluid Mechanics* 649:287–328
- 315 Gunn A, Wanker M, Lancaster N, Edmonds DA, Ewing RC, Jerolmack DJ
316 (2021) Circadian rhythm of dune-field activity. *Geophysical Research Letters*
317 48(5):e2020GL090,924
- 318 Hersbach H, Bell B, Berrisford P, Hirahara S, Horányi A, Muñoz-Sabater
319 J, Nicolas J, Peubey C, Radu R, Schepers D, et al. (2020) The era5
320 global reanalysis. *Quarterly Journal of the Royal Meteorological Society*
321 146(730):1999–2049
- 322 Hesp PA, Smyth TAG, Nielsen P, Walker IJ, Bauer BO, Davidson-Arnott R
323 (2015) Flow deflection over a foredune. *Geomorphology* 230:64–74
- 324 Hunt JCR, Vilenski GG, Johnson ER (2006) Stratified separated flow around
325 a mountain with an inversion layer below the mountain top. *Journal of Fluid
326 Mechanics* 556:105–119
- 327 Jiang Q (2014) Applicability of reduced-gravity shallow-water theory to
328 atmospheric flow over topography. *Journal of the Atmospheric Sciences*
329 71(4):1460–1479
- 330 Lancaster LNSM J (1984) Climate of the central namib desert. *Madoqua*
331 1984(1):5–61
- 332 Lancaster N (1985) Winds and sand movements in the namib sand sea. *Earth
333 Surface Processes and Landforms* 10(6):607–619
- 334 Muñoz-Sabater J, Dutra E, Agustí-Panareda A, Albergel C, Arduini G, Bal-
335 samo G, Boussetta S, Choulga M, Harrigan S, Hersbach H, et al. (2021)
336 Era5-land: A state-of-the-art global reanalysis dataset for land applications.

- 337 Earth System Science Data Discussions pp 1–50
- 338 Pähzt T, Durán O (2020) Unification of aeolian and fluvial sediment transport
339 rate from granular physics. *Physical review letters* 124(16):168,001
- 340 Seidel DJ, Zhang Y, Beljaars A, Golaz JC, Jacobson AR, Medeiros B (2012)
341 Climatology of the planetary boundary layer over the continental united
342 states and europe. *Journal of Geophysical Research: Atmospheres* 117(D17)
- 343 Sheridan PF, Vosper SB (2006) A flow regime diagram for forecasting lee
344 waves, rotors and downslope winds. *Meteorological Applications* 13(2):179–
345 195
- 346 Smith AB, Jackson DWT, Cooper JAG (2017) Three-dimensional airflow and
347 sediment transport patterns over barchan dunes. *Geomorphology* 278:28–42
- 348 Stull RB (1988) An introduction to boundary layer meteorology, vol 13.
349 Springer Science & Business Media
- 350 Sullivan PP, McWilliams JC (2010) Dynamics of winds and currents coupled
351 to surface waves. *Annual Review of Fluid Mechanics* 42:19–42
- 352 Tritton D (2012) Physical fluid dynamics. Springer Science & Business Media
- 353 Vosper SB (2004) Inversion effects on mountain lee waves. *Quarterly Journal
354 of the Royal Meteorological Society: A journal of the atmospheric sciences,
355 applied meteorology and physical oceanography* 130(600):1723–1748

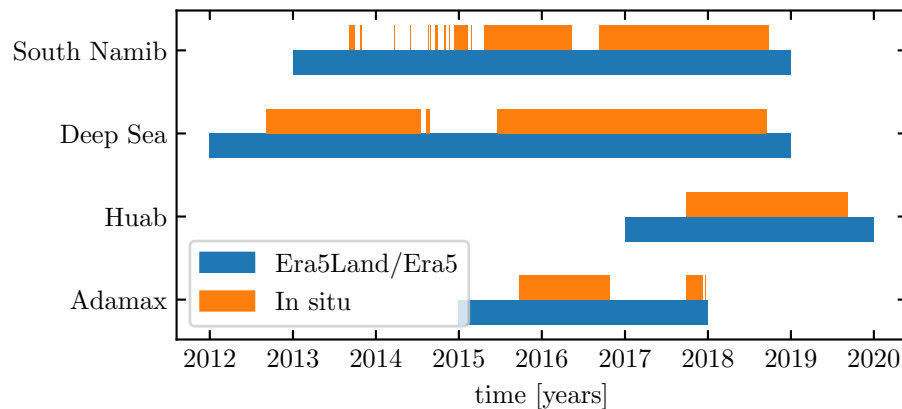


Fig. S1 Gant chart representing the usable time steps for the two data sets, for all stations.

356 **Supplementary Material for *Boundary-Layer Meteorology* Sample
357 Paper: Instructions for Authors**

358 **First Author* · Second Author · Third Author**

359
360 *Affiliation and email address for the corresponding author only (note that
361 the corresponding author does not need to be the first author).

362 **1. Calibration of the hydrodynamical roughness**

363 For each station, the hydrodynamic roughness is calibrated by finding the
364 one that minimizes the relative difference δ between the wind vectors of both
365 datasets:

$$\delta = \frac{\sqrt{\langle \|u_{*,\text{era}} - u_{*,\text{station}}\|^2 \rangle_t}}{\sqrt{\langle \|u_{*,\text{era}}\| \rangle_t \langle \|u_{*,\text{station}}\| \rangle_t}} \quad (16)$$

366 This δ -parameter is computed for hydrodynamic roughness values ranging
367 from 10^{-5} m to 10^{-2} m for the different stations. As shown by figure S3,
368 the minimum of δ in the space ($z_0, \text{Era}, z_0, \text{in situ}$) forms a line. We thus take
369 the roughness of the Era5Land dataset as the typical value when sediment
370 transport occurs, 10^{-3} m, corresponding to the thickness of the transport
371 layer (?). It leads for the Adamax, Deep Sea, Huab and South Namib stations
372 values of 2.7 mm, 0.76 mm, 0.12 mm and 0.48 mm, respectively.

373 The choice of the hydrodynamic roughness values only impacts the cal-
374 culated shear velocities, but note the wind directions. As such, most of our
375 conclusions are then independent of such a choice, and only the magnitude of
376 the wind velocity attenuation in confined situation might be affected.

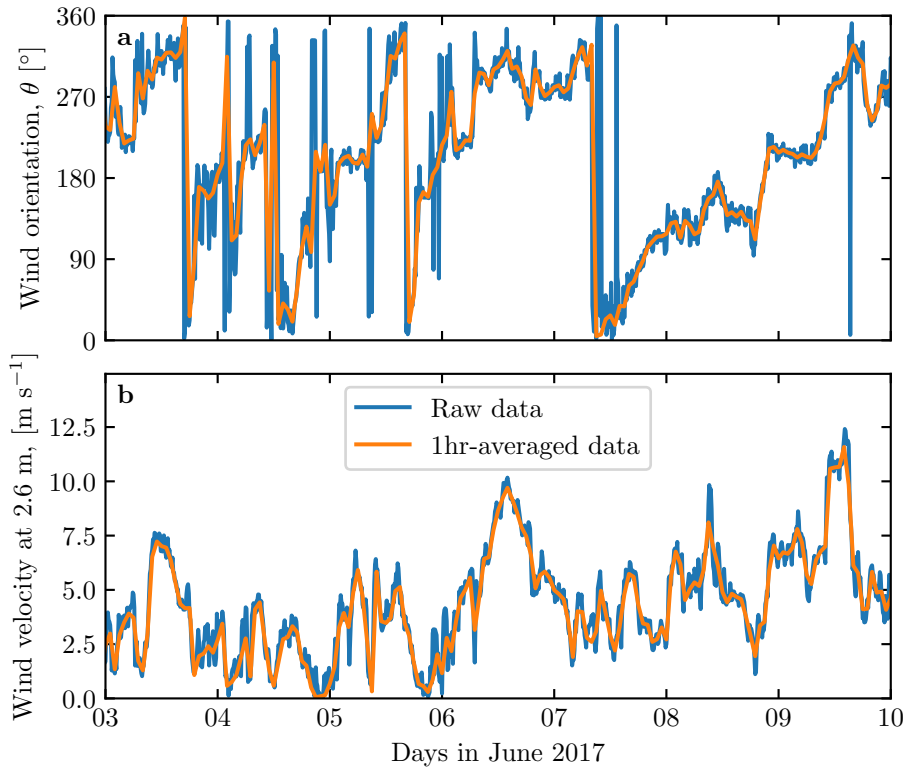


Fig. S2 Comparison between raw in situ wind measurements, and centered averaged data over one hour for the South Namib station. **a:** wind direction. **b:** wind velocity at the measurement height, 2.6 m.

377 2. Extraction of the ABL properties

378 In order to estimate the relevant non-dimensional numbers, one need to es-
 379 timate in addition to the wind and dune properties some parameters of the
 380 ABL. The Era5 dataset provides a direct bulk estimate of the ABL depth H
 381 from a bulk Richardson number calculation, as well as vertical profiles of the
 382 geopotential ϕ , temperature T and specific humidity e_w at given pressure lev-
 383 els P . From these quantities, the virtual potential temperature, which takes
 384 into account the vertical pressure and humidity changes, can be calculated as:

$$T_{vp} = T (1 + [R_M - 1] e_w) \left(\frac{P_0}{P} \right)^{P_c(1-0.24e_w)}, \quad (17)$$

385 where $P_0 = 10^5$ Pa is the standard pressure, $P_c = 0.2854$ the Poisson coefficient
 386 for dry air and $R_M = 1.61$ is the ratio between the molecular masses of dry
 387 air and water. The vertical coordinates are calculated as:

$$z = \frac{\phi R_t}{g R_t - \phi}, \quad (18)$$

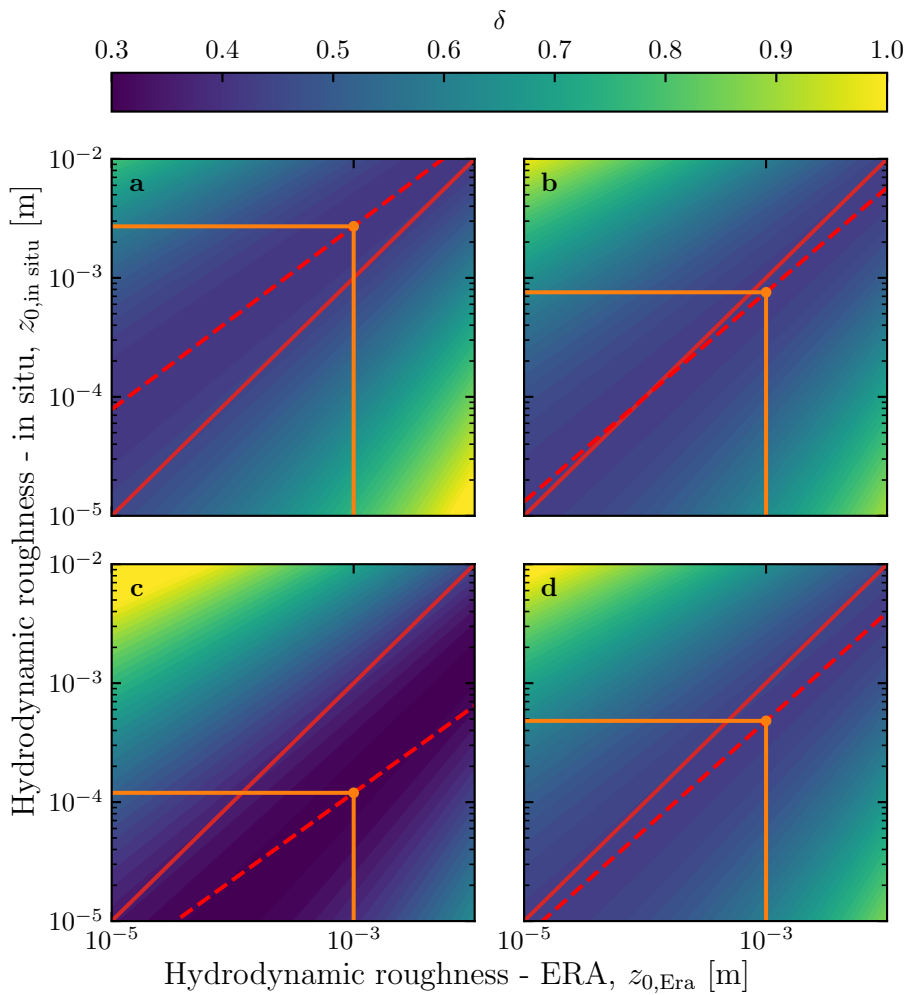
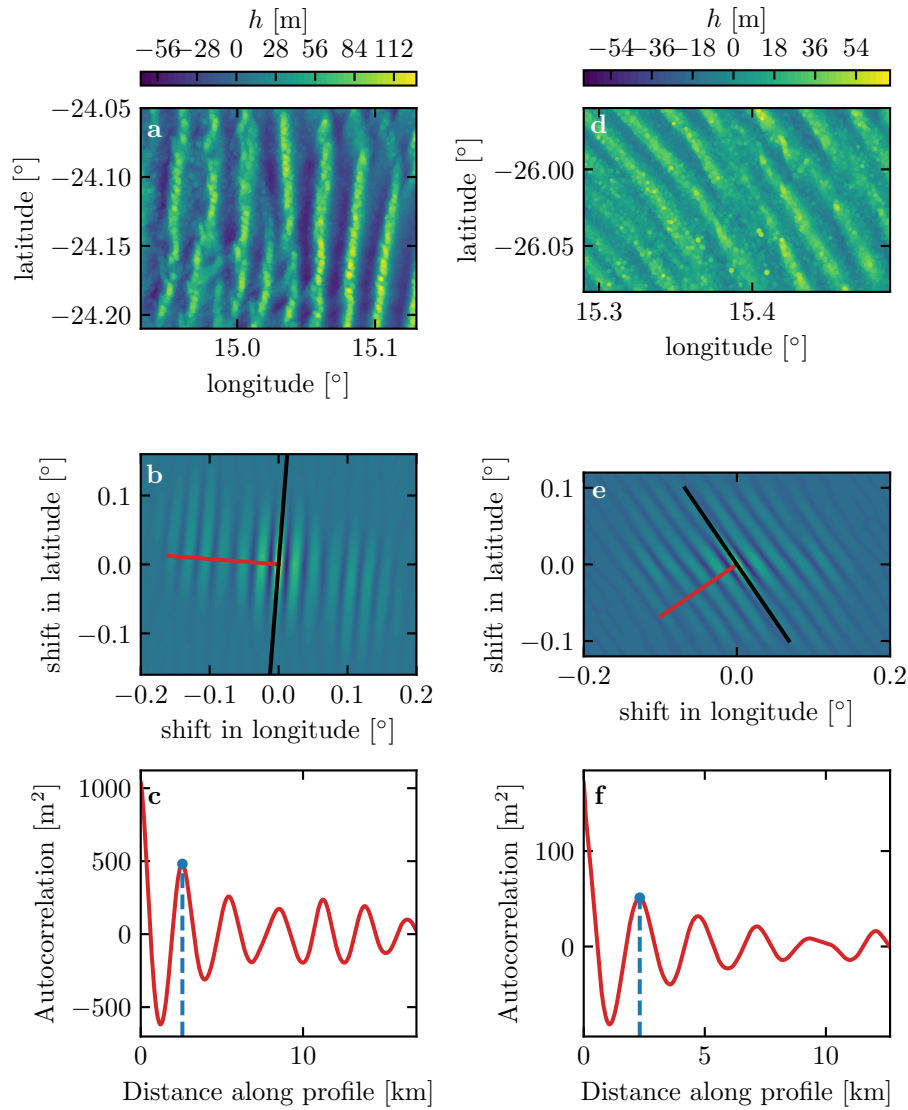


Fig. S3 Calibration of the hydrodynamic roughnesses. The metric δ defined in (16) is represented in colorscale as a function of the hydrodynamic roughnesses chosen for the Era5-Land and in situ datasets, for the Adamax (**a**), Deep Sea (**b**), Huab (**c**) and South Namib (**d**) Stations. The red dashed and plain lines shows the minima of δ and the identity line. The orange lines and dots highlights the chosen the hydrodynamic roughnesses for the in situ datasets by imposing $z_{0,\text{ERA}} = 1 \text{ mm}$, leading for each station to 2.7 mm, 0.76 mm, 0.12 mm and 0.48 mm, respectively.

388 where $R_t = 6356766 \text{ m}$ is the average Earth radius, and $g = 9.81 \text{ m s}^{-2}$ the
389 gravitational acceleration.

390 Example of obtained vertical profiles of the virtual potential temperature
391 are shown in Fig. S9. On each of them, an average is computed below the ABL
392 depth given by the Era5 dataset, and a linear function is fitted above.

393 Under the Boussinesq approximation, the temperature variations are as-
394 sumed to induce most of those of the density, leading to $\Delta\rho/\rho \simeq \Delta T_{\text{vp}}/T_{\text{vp}}$.



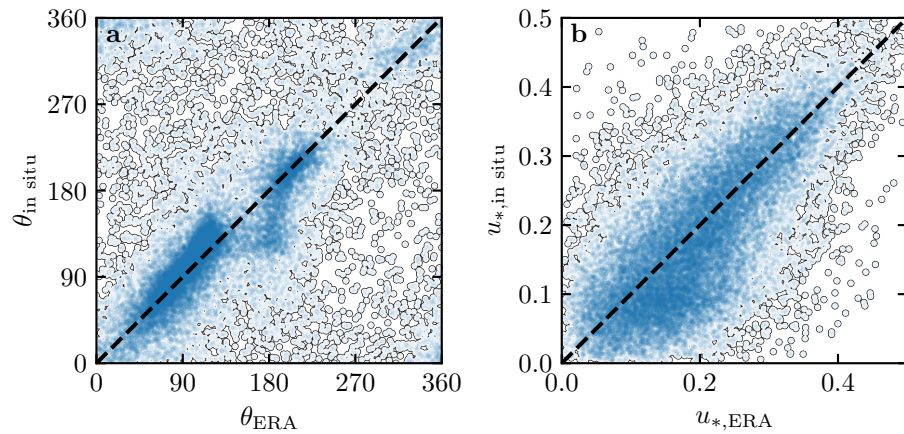


Fig. S5 Statistical agreement of the wind orientation (a) and velocity (b) between the Era5Land dataset and the in situ measurements for the Huab and Adamax stations. Note how the points are clustered around identity lines, black and dashed.

395 Here, $T_{\text{vp}}/T_{\text{vp}}$ is the relative virtual potential temperature jump at the cap-
 396 ping, directly measured on the vertical profiles.

397 Following Tritton (2012), the relative density jump at the capping layer

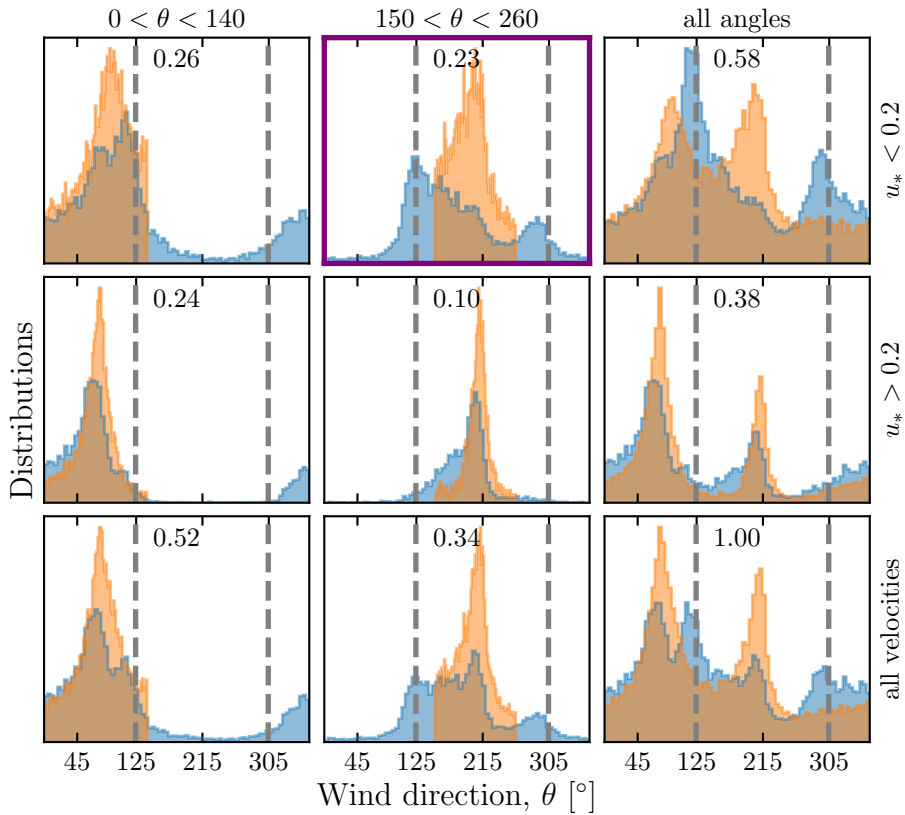


Fig. S6 Distributions of wind direction at the South Namib Station for the Era5Land climate reanalysis (orange) and the in situ measurements (blue). In each subplot, both distributions are plotted from the same time steps, selected with constraints on the wind direction (columns) and/or wind velocity (rows) in the Era5Land dataset. The grey dashed vertical lines indicate the dune orientation. The purple frame highlights the regime (small wind velocities, nocturnal summer wind) during which the wind data from both datasets differs. A similar figure can be obtained for the South Namib station (see Fig. 3).

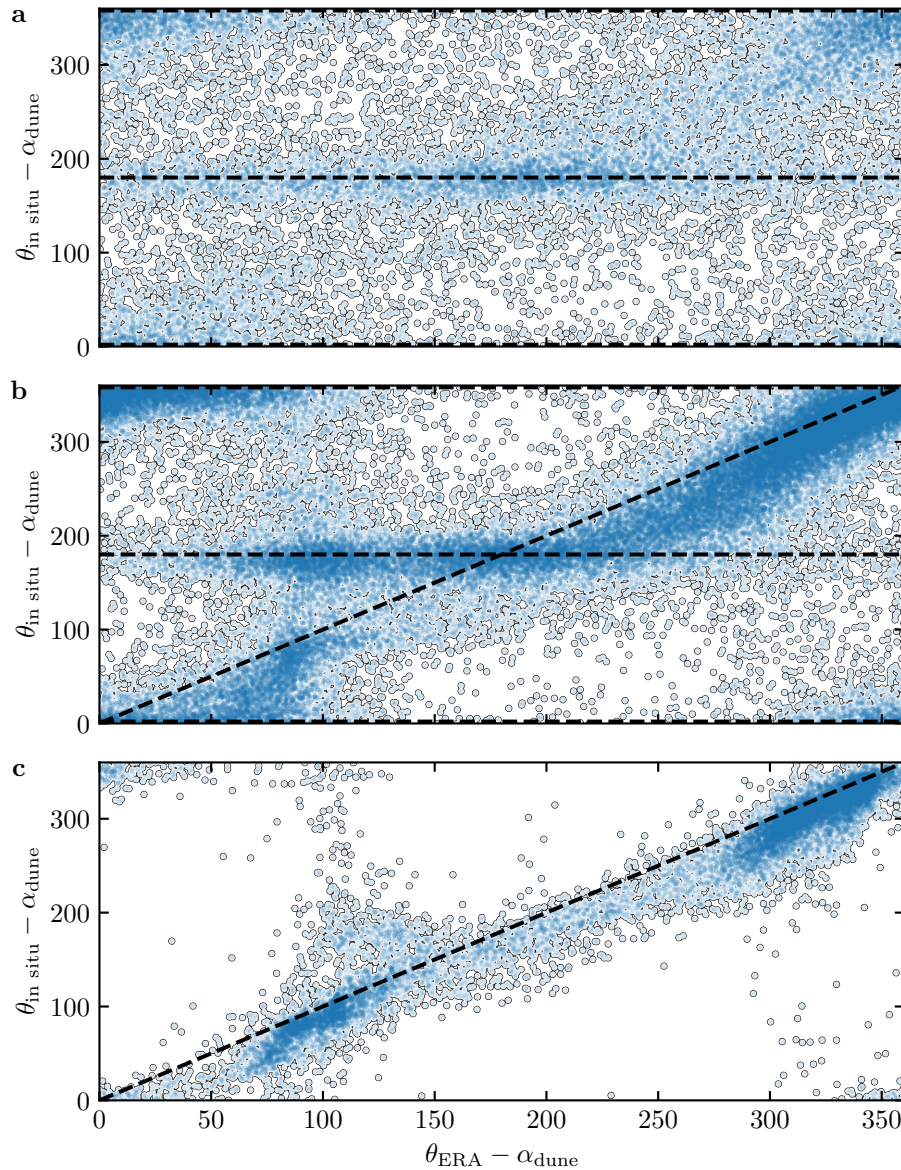


Fig. S7 Statistical comparison of the wind orientation between the Era5Land dataset and in situ measurements for the South Namib and Deep Sea stations, for different velocity ranges. **a:** $u_{*,\text{ERA}} < 0.1 \text{ m s}^{-1}$. **b:** $0.1 < u_{*,\text{ERA}} \leq 0.25 \text{ m s}^{-1}$. **c:** $u_{*,\text{ERA}} \geq 0.25 \text{ m s}^{-1}$. Note that the dune orientations measured are subtracted to the wind orientation, which allows to plot both stations on the same graph. Black dashed lines indicates in situ orientations aligned with the dune crests (here 0° , 180° and 360° – **a, b**), as well as the identity lines (**b, c**).

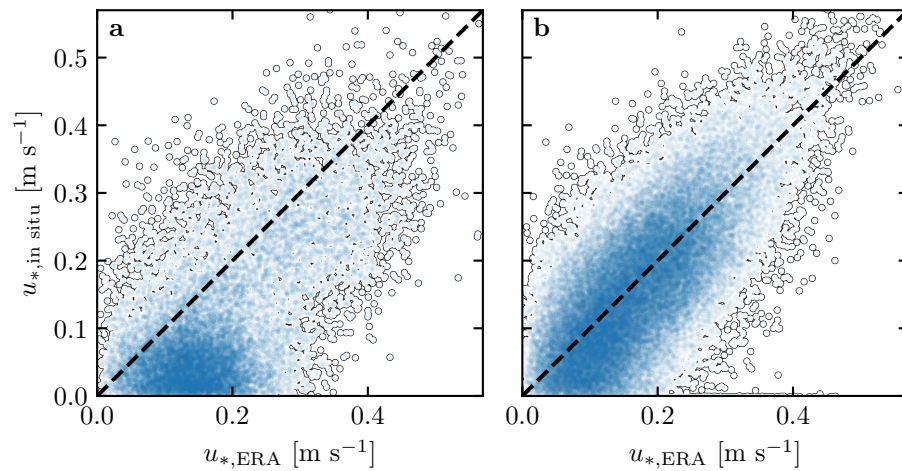


Fig. S8 Statistical comparison of the wind velocity between the Era5Land dataset and in situ measurements for the South Namib and Deep Sea stations. **a:** Nocturnal summer easterly wind. **b:** Diurnal southerly wind. Black dashed lines are identity lines. The angle ranges corresponding to diurnal and nocturnal summer winds are those taken in Fig. 3 and Fig. S6.

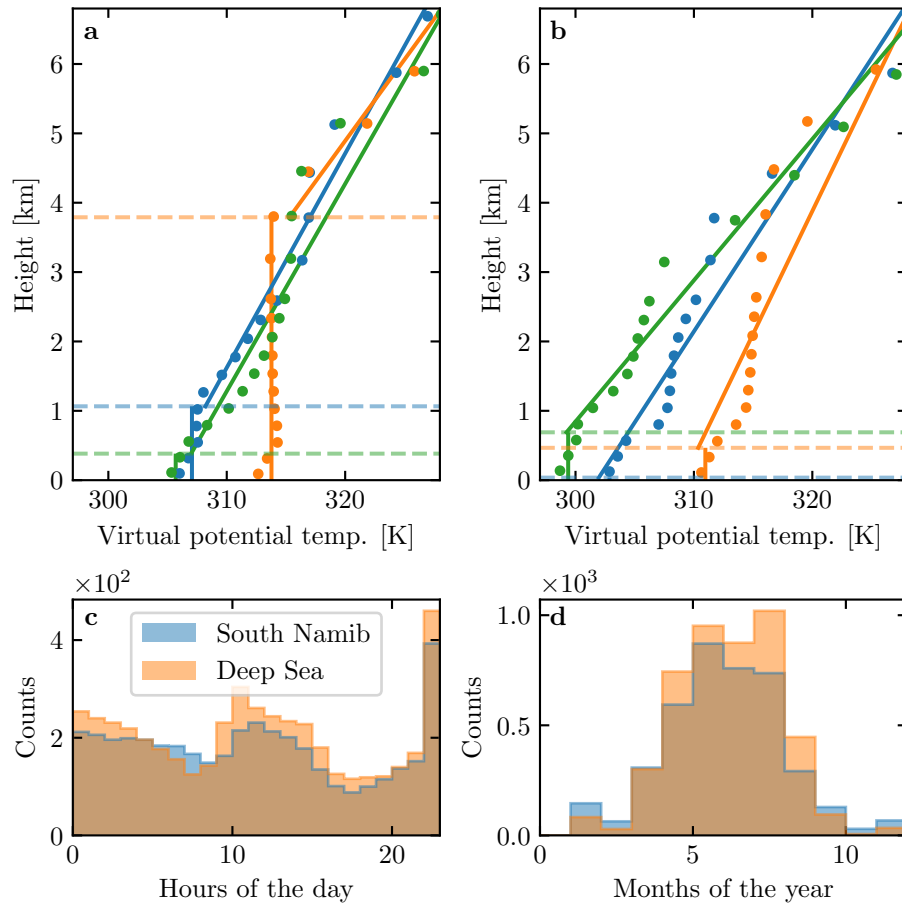


Fig. S9 **a:** Vertical profiles of the virtual potential temperature at 3 different time steps (blue - 29/11/2012 - 1100 UTC, orange - 21/03/2017 - 1200 UTC, green - 21/03/2017 - 2000 UTC) at the South Namib station. Dots: data from the ERA5 reanalysis. Transparent dashed lines: boundary layer height given by the ERA5 reanalysis, calculated from the bulk Richardson number (Seidel et al. 2012). Plain lines: vertical (boundary layer) and linear (free atmosphere) fits to estimate the quantities in Fig. S10. **b:** Examples of ill-processed vertical profiles at 3 different time steps (blue - 2/12/2013 - 2300 UTC, orange - 20/03/2017 - 0000 UTC, green - 14/07/2017 - 1400 UTC) at the South Namib station. **c:** Hourly distribution of ill-processed vertical profiles. **d:** Monthly distribution of ill-processed vertical profiles. These profiles are ill-processed because the temperature found at the boundary layer from the linear fit in the free-atm is smaller than the average one inside the boundary layer. This is an unstable situation, which does not allow to calculate the surface Froude number.

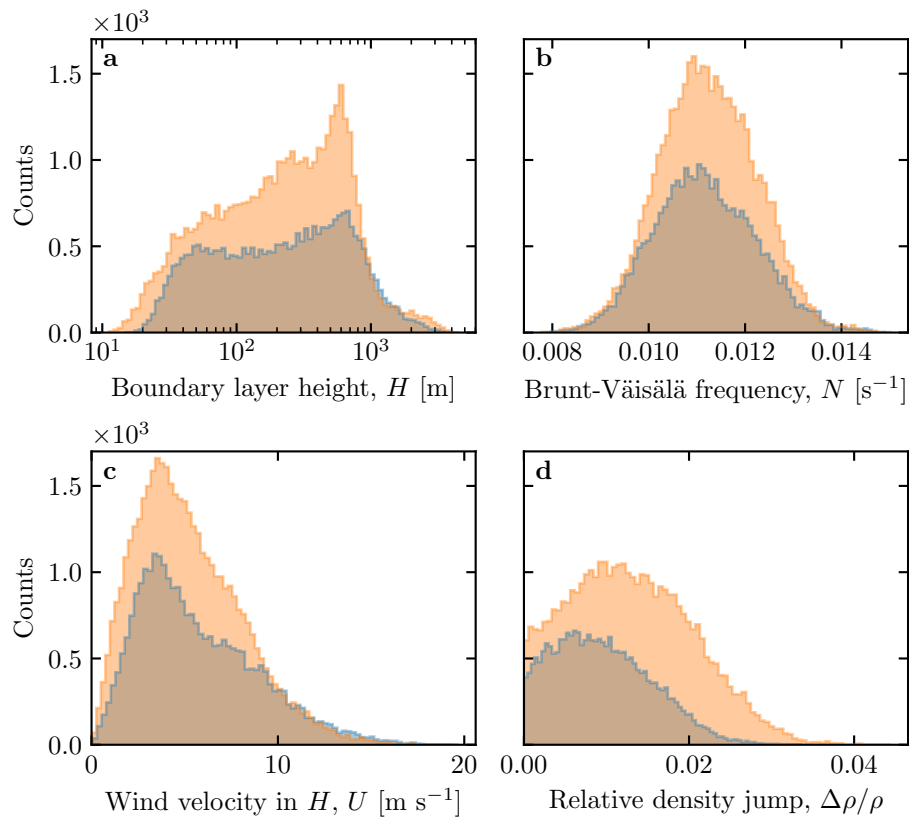


Fig. S10 Distributions of the meteorological parameters resulting from the processing of the Era5-Land data for the South Namib (blue) and the Deep Sea (orange) stations.

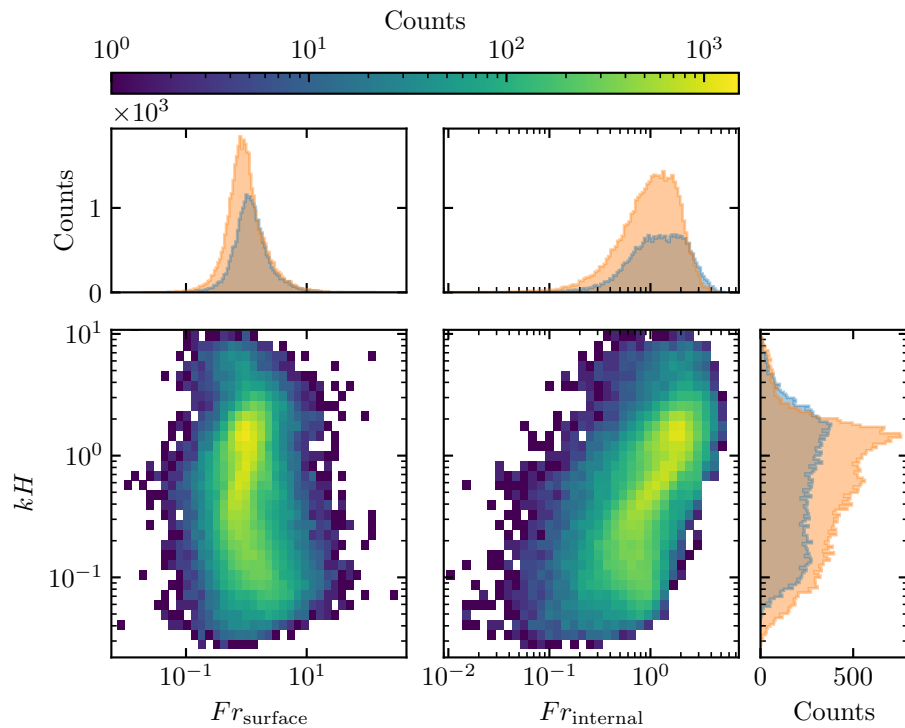


Fig. S11 Non-dimensional parameters distributions. For the marginal distributions, the orange correspond to the South Namib station, and the blue to the Deep Sea station.

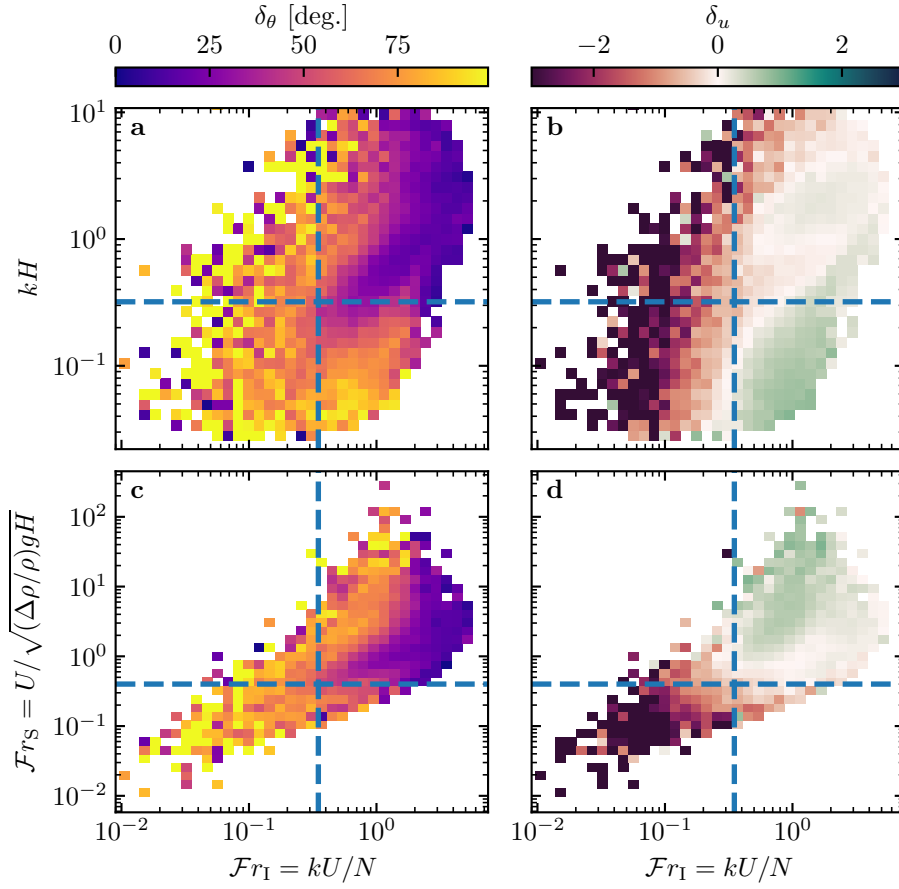


Fig. S12 Regime diagrams of the wind deviation δ_θ and relative attenuation/amplification δ_u in the spaces (\mathcal{Fr}_I, kH) and $(\mathcal{Fr}_I, \mathcal{Fr}_S)$, containing the data from both the Deep Sea and South Namib stations. Blue dashed lines empirically delimit the different regimes. The point density in each bin of the diagrams is shown in Fig. S11. The regime diagrams in the space (\mathcal{Fr}_S, kH) are shown in Fig. S5.

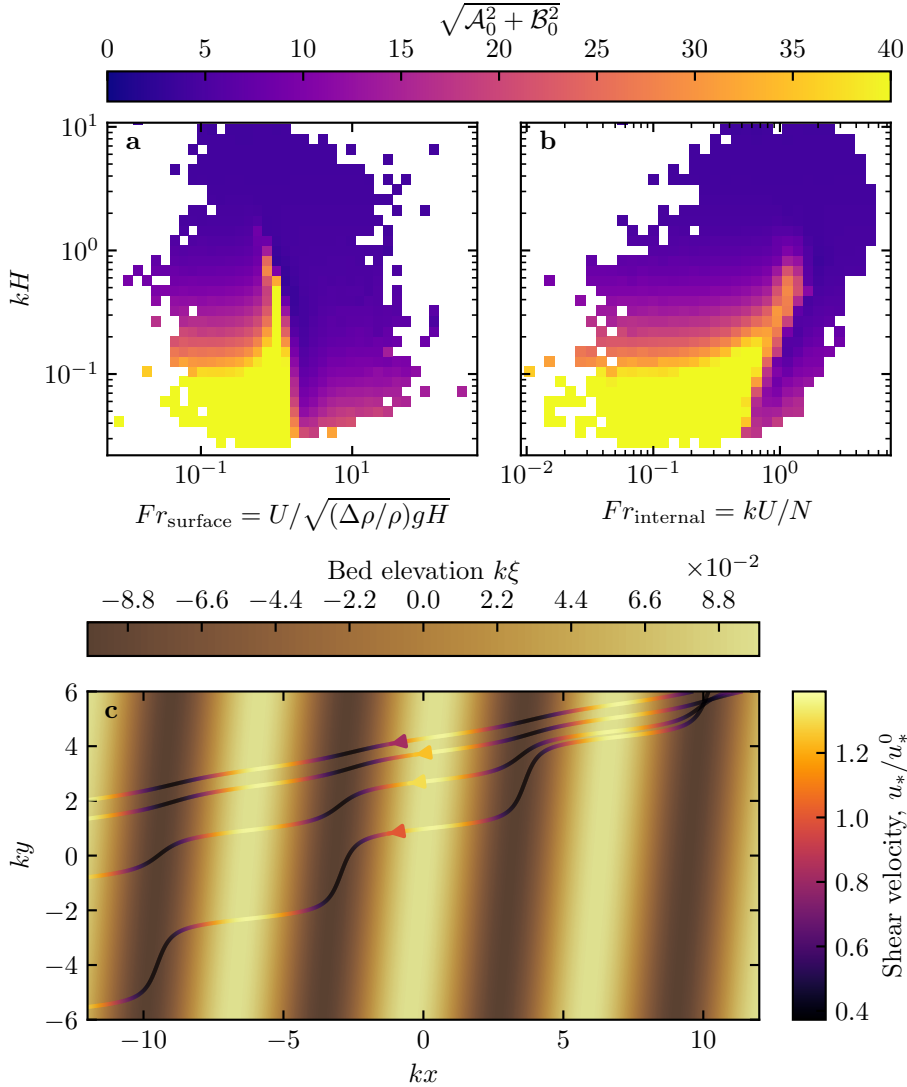


Fig. S13 Physical interpretation of the flow disturbance. (a) and (b) Magnitude of the disturbance induced by a sinusoidal topography calculated from the time series of the non-dimensional numbers presented in Figures 4 and 5 using the linear model of Andreotti et al. (2009). (c) Shear velocity streamlines represented in the case of the Deep Sea station, for increasing values of $\sqrt{\mathcal{A}_0^2 + \mathcal{B}_0^2}$. From the upper to the lower streamline, values of $(kH, Fr_{\text{surface}}, Fr_{\text{internal}}, \mathcal{A}_0, \mathcal{B}_0, \sqrt{\mathcal{A}_0^2 + \mathcal{B}_0^2})$ are $(1.9, 0.6, 1.5, 3.4, 1.0, 3.5)$, $(1.5, 0.3, 0.4, 4.8, 1.4, 5.0)$, $(0.1, 3.5, 1.0, 8.6, 0.1, 8.6)$, $(0.5, 0.05, 0.04, 9.6, 2.5, 9.9)$.